



Hydrogen production by photocatalytic steam reforming of methanol on noble metal-modified TiO₂

Gian Luca Chiarello^a, Myriam H. Aguirre^b, Elena Selli^{a,*}

^a Dipartimento di Chimica Fisica ed Elettrochimica, CIMAINA and ISTM-CNR, Università degli Studi di Milano, Via Golgi 19, I-20133 Milano, Italy

^b Empa – Swiss Federal Laboratories for Materials Testing and Research Solid State Chemistry and Catalysis, Ueberlandstrasse 129, CH-8600 Dübendorf, Switzerland

ARTICLE INFO

Article history:

Received 9 March 2010

Revised 22 April 2010

Accepted 21 May 2010

Available online 29 June 2010

Keywords:

Photocatalytic H₂ production

Photo-steam reforming

Methanol

Flame spray pyrolysis

Noble metals on TiO₂

ABSTRACT

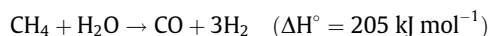
The photocatalytic production of hydrogen by methanol steam reforming was studied over a series of pristine or noble metal (Ag, Au, Au–Ag alloy and Pt) – modified TiO₂ photocatalysts, synthesised by flame spray pyrolysis or by the deposition of preformed noble metal nanoparticles on TiO₂. A closed recirculation apparatus was employed, with the photocatalyst bed continuously fed with methanol/water vapours. Methanol underwent oxidation up to CO₂ through the formation of formaldehyde and formic acid. Carbon monoxide, methane, methyl formate, acetaldehyde and dimethyl ether were identified as side products. Hydrogen evolved at constant rate, which significantly increased upon noble metal addition, Pt being the most effective co-catalyst, followed by gold and silver, according to their work function values. A systematic investigation into the effects of the inlet gas composition gave valuable information on the prevailing reaction paths and on the conditions of process optimisation, also in terms of distribution of CH₃OH oxidation products.

© 2010 Elsevier Inc. All rights reserved.

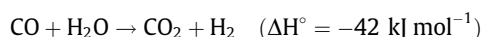
1. Introduction

Hydrogen is widely considered the clean energy vector of the future. However, nowadays, about two-thirds of the world's hydrogen production is employed in ammonia synthesis to produce fertilizers; large amounts are used in the synthesis of methanol, by reaction with carbon monoxide, and in the catalytic hydrogenation of organic compounds [1].

Although the technologies of energy production from hydrogen, e.g. fuel cells and internal hydrogen combustion engines, are already mature, hydrogen production remains a major problem. Indeed, nearly all hydrogen production is still based on fossil raw materials, and only 4% is produced *via* water electrolysis. The most important industrial route of hydrogen production consists in the catalytic steam-reforming of hydrocarbons, implying gaseous or vaporised hydrocarbons treatment with steam at high pressure (15–40 bar) and high temperature (650–950 °C) over nickel-based catalysts. In the case of methane, the reaction is as follows:



Additional hydrogen can be recovered by a subsequent, lower temperature “water gas shift” step, in which steam further oxidises CO yielding CO₂:



Because of the endothermic nature of the steam reforming reaction, heat must be supplied for the reaction to proceed, and this is usually provided by the combustion of part of the feed stock, with a consequent decrease in the net yield of the process.

The recent growing concern about global climate change, mainly tied to the exploitation of fossil fuels, led to great efforts in the development of new alternative, environmentally friendly energy sources. The photocatalytic production of hydrogen from photo-reforming of biomass on metal oxide semiconductors can respond to this urgent need. Indeed, since biomasses are renewable and consume atmospheric CO₂ during their growth, they have a small net CO₂ impact compared to fossil fuels.

Photocatalytic reactions on semiconductors are initiated by the absorption of photons with energy $h\nu$ equal to, or greater than, the semiconductor band gap [2]. This promotes an electron from the valence band (VB) to the conduction band (CB), with the consequent formation of an electron (e_{CB}^-)–hole (h_{VB}^+) pair. The so produced charge carriers can induce the reduction of electron acceptor species, having a reduction potential lower in energy than the CB, and the oxidation of electron donor species, having a reduction potential higher in energy than the VB, respectively. In the case of the photo-reforming reaction, H⁺ ions are the electron acceptors, and the organic substrates, which are oxidised up to CO₂, are the electron donors. The overall reaction is endoergonic and can be regarded as a sort of artificial photosynthesis, able to convert radiation energy into chemical energy, *i.e.* into H₂. Contrarily to traditional steam reforming, the photo-assisted process occurs at room temperature and atmospheric pressure and no feed

* Corresponding author. Fax: +39 02 503 14300.

E-mail address: elena.selli@unimi.it (E. Selli).

stock needs to be burnt, because the required energy is totally supplied by photons. With photocatalysts able to absorb solar light efficiently, the process represents a fascinating way of harvesting and converting solar energy.

Although different mixed metal oxide semiconductors, also with rather complex structure, have been proposed as photocatalysts in recent years [3–7], titanium dioxide modified by noble metal nanoparticles still remains the best photocatalyst for hydrogen production [8,9]. Indeed, the Fermi level of noble metals is usually lower in energy than the conduction band energy of the TiO₂ semiconductor. Thus, photopromoted electrons can migrate and be captured by the noble metal, whereas photoproduced holes remain in the TiO₂ valence band. The rate of photocatalytic hydrogen production is further increased in the presence of organic compounds able to act as hole scavengers, undergoing relatively rapid and irreversible oxidation on the TiO₂ surface. Of course, also, organics deriving from renewable sources, *i.e.* biomasses, may be profitably employed as hole scavengers. For instance, methanol is widely used as a sacrificial agent in the liquid-phase photocatalytic production of hydrogen [10–13].

However, the photo-steam reforming reaction did not receive much attention so far. Steam addition was found to increase methanol conversion in the gas-phase anaerobic photocatalytic oxidation of methanol over Fe/TiO₂ [14]. Greaves et al. [13] evidenced an increase in hydrogen production rate when an Au/TiO₂ photocatalyst film was illuminated in contact with methanol–water vapours, with respect to the same photocatalyst in liquid suspension. The photocatalytic steam reforming of methane has been recently investigated by Yoshida et al. [15] employing Pt/TiO₂ in a flow reactor.

In the present work, a systematic investigation has been performed on hydrogen production by photocatalytic steam reforming of methanol, employed as a volatile and simple organic electron donor acting as sacrificial reagent able to combine with photoproduced holes, in a model reaction for photocatalytic hydrogen formation from renewable sources. A series of noble metal (NM) containing TiO₂-based photocatalysts has been employed, either synthesised in a single and continuous step by flame spray pyrolysis (FP) [16], according to a procedure leading to very photoactive high surface area titania, also modified with noble metals nanoparticles [17,18], or obtained by the deposition of preformed noble metals (Ag, Au, Au–Ag alloy and Pt) nanoparticles on TiO₂. Particular attention has been made on the identification of all photoreaction intermediates and by-products and on their production rates, also as a function of the inlet gas composition, aiming at identifying the main reaction paths and at ascertaining which photocatalyst features are required to optimise the process, not only in terms of hydrogen yield, but also in terms of distribution of CH₃OH oxidation products.

2. Experimental

2.1. Photocatalysts preparation

The investigated photocatalysts are listed in Table 1. They were all home-prepared, apart from P25 TiO₂ from Degussa, frequently employed as benchmark in photocatalytic studies. FP-TiO₂ and FP-0.5 wt.%Pt/TiO₂ were synthesised in a continuous and single step by the already described FP method [16], starting from a solution containing 10 mL of titanium(IV)-isopropoxide dissolved in a xylene (35 mL)/acetonitrile (5 mL) mixture, also containing the required amount of platinum precursor (Pt acetylacetonate), when necessary. The so obtained solution was fed at constant rate (4 mL min⁻¹) to the flame reactor, together with oxygen (5 L min⁻¹). The solution was so sprayed and ignited by a crown of twelve methane/oxygen supporting flamelets surrounding the central nozzle of the reactor, forming a vertical main flame in which the photocatalyst nanoparticles were produced. The obtained powder was then collected on the electrodes of an electrostatic precipitator.

The series of 1.0 (or 0.5) wt.% NM/TiO₂ (NM = Ag, Au and Pt) photocatalysts, as well as the photocatalyst containing an Au/Ag alloy (*i.e.* sample 1%Au–1%Ag/TiO₂), were synthesised by the deposition of surfactant-stabilised preformed NM nanoparticles on commercial TiO₂ Degussa P25 or on FP-TiO₂ (sample 0.5%Pt/FP-TiO₂), adopting a reverse micelle method similar to that described by Liu et al. [19]. Chloroauric acid, hexachloroplatinic acid and silver nitrate were used as NM precursors. Proper amounts of NM precursor were dissolved in 95 mL of an *n*-dodecyltrimethylammonium chloride aqueous solution, to obtain a 40:1 surfactant to NM molar ratio. NM colloidal suspensions were then obtained by adding 5 mL of a NaBH₄ aqueous solution (4:1 NaBH₄ to NM molar ratio) under vigorous stirring. The colour turned from yellowish to deep dark, as a consequence of NM reduction. The proper amount of TiO₂ powder, dispersed in water (50 mL) in an ultrasonic bath, was then added to the NM colloidal suspension under vigorous stirring. When stirring was stopped, a coloured powder was precipitated, whereas the supernatant liquid was perfectly clear, indicating the total deposition of the NM colloids on the TiO₂ surface. Finally, the powder was recovered after at least four cycles of precipitation, supernatant separation and washing with water. The final wet precipitated powder was centrifuged to minimise its water content and dried overnight in oven at 70 °C. All chemicals were purchased from Aldrich and used as received.

2.2. Photocatalysts characterisation

The BET-specific surface area was measured by N₂ adsorption/desorption at 77 K on a Micromeritics ASAP 2010 apparatus, after out-gassing *in vacuo* at 300 °C for at least 6 h. X-ray diffraction pat-

Table 1

Photocatalytic performance of the investigated photocatalysts in methanol photo-steam reforming, in terms of rates of products formation, *r*, and per cent selectivity in relation to hydrogen production, *S*. Reaction conditions: 0.014 g of photocatalyst fed in recirculation mode with 40 mL min⁻¹ of a 2% CH₃OH/3% H₂O/N₂ (balance) gas mixture.

Photocatalyst	Production rate (mmol h ⁻¹ g _{cat} ⁻¹)						Selectivity in relation to H ₂ production (%)				
	H ₂	CO ₂	CO	H ₂ CO	HCO ₂ H	CH ₄	CO ₂	CO	H ₂ CO	HCO ₂ H	Sum
TiO ₂	0.36	0.013	0.032	0.25	tr.	9.1 × 10 ⁻⁴	10.7	17.7	69.4	–	98
FP-TiO ₂	0.72	0.022	0.044	0.48	tr.	7.6 × 10 ⁻⁴	9.1	12.2	67.0	–	88
1%Ag/TiO ₂	1.17	0.032	0.056	0.81	0.06	1.1 × 10 ⁻³	8.2	9.6	68.8	11.0	98
1%Au/TiO ₂	13.30	1.61	0.479	5.17	0.84	1.2 × 10 ⁻³	36.3	7.2	38.9	12.7	95
1%Au–1%Ag/TiO ₂	12.82	1.24	0.603	5.23	1.11	1.6 × 10 ⁻³	29.0	9.4	40.8	17.3	96
1%Pt/TiO ₂	18.60	2.88	0.468	7.16	1.23	8.7 × 10 ⁻³	46.4	5.0	38.5	13.2	103
0.5%Pt/TiO ₂	7.75	0.45	0.322	4.40	0.58	4.4 × 10 ⁻³	17.5	8.3	56.7	14.9	98
0.5%Pt/FP-TiO ₂	8.36	0.70	0.190	4.65	0.49	2.8 × 10 ⁻³	25.1	4.6	55.6	11.8	97
FP-0.5%Pt/TiO ₂	14.23	1.02	0.078	7.85	1.44	2.3 × 10 ⁻³	21.6	1.1	55.1	20.3	98

terns were recorded on a Philips PW3020 powder diffractometer, by using the Cu K α radiation ($\lambda = 1.54056 \text{ \AA}$) and compared with literature data [20] for phase recognition. Quantitative phase analysis was made by the Rietveld refinement method [21], using the “Quanto” software [22]. UV–vis diffuse reflectance was measured by a Perkin-Elmer Lambda 35 apparatus equipped with an integration sphere (Labsphere RSA-PE-20).

High Resolution Transmission Electron Microscopy (HRTEM) and High Angular Annular Dark Field image in Scanning mode (STEM–HAADF) were taken on a JEOL FS2200-FEG operating at 200 kV. The catalysts were dispersed in ethanol, dropped on carbon-film coated copper grids and dried in air. In STEM and EDX (Energy Dispersive X-ray) analysis the spot size was 0.7 nm. The 3.7.0 analysis station with the JED-2200 software from Jeol was used to process EDX spectra.

2.3. Photocatalytic tests

The photocatalytic activity in hydrogen production by methanol photo-steam reforming was tested using an apparatus similar to that already described [18]. The photocatalyst powder (14 mg) was deposited on 3 g of 20–40 mesh (0.85–0.42 mm) quartz beads by mixing them with 1.2 mL of distilled water, followed by drying in oven at 70 °C for 6 h. The so obtained photocatalyst bed was inserted in the photoreactor, consisting in a flat cylindrical Plexiglas cell, having a central 2 mm thick and 50 mm in diameter round hollow, frontally closed with a Pyrex glass optical window (irradiation surface *ca.* 20 cm²). The photoreactor was connected to a closed stainless steel system, where the gas phase was recirculated at constant rate by means of a metal bellows pump. The system was preliminarily purged with nitrogen in order to remove any oxygen trace. During the photocatalytic tests, the inert gas was saturated with methanol/water vapours by continuously bubbling it into an aqueous solution containing different methanol amounts, kept at 30 °C, and then fed to the photoreactor. In particular, the photocatalytic activity tests of different photocatalysts were carried out employing 20 vol.% methanol in water solutions (standard conditions), whereas different solutions containing from 1 vol.% up to pure methanol were employed when investigating the effect of methanol content. The photocatalyst bed was typically irradiated for 2 h, while the recirculating gas was analysed on-line by sampling it every 20 min by means of a pneumatic sampling valve placed at the exit of the photoreactor. Gas samples were automatically injected into an Agilent 6890 N gas-chromatograph (GC), equipped with two columns (HP-PlotU and Molesive 5A), two detectors (thermo conductivity and flame ionisation) and a Ni-catalyst kit for CO and CO₂ methanation. N₂ was used as carrier gas. The GC response was first calibrated by injecting known volumes of H₂, CO, CO₂ and CH₄ into the recirculation system through the loop of a six ways sampling valve. The amount of formic acid accumulated in the liquid solution during the photocatalytic tests was determined by ion chromatography (IC), employing a Metrohm 761 Compact IC instrument equipped with an anionic Metrosep A column.

The irradiation source was an iron halogenide mercury arc lamp (Jelosil, 250 W), placed at 20 cm from the reactor, emitting in the 350–450 nm wavelength range with a full irradiation intensity of $1.67 \times 10^{-7} \text{ Einstein s}^{-1} \text{ cm}^{-2}$ on the reactor, as determined by ferrioxalate actinometry [23]. Its constancy was checked daily by an UVA-meter, giving a constant reading of 37 mW cm^{-2} at 20 cm from the lamp.

The reactor temperature during irradiation was $55 \pm 5 \text{ }^\circ\text{C}$, as monitored by a thermocouple placed inside the cell. The absolute pressure was 1.2 bar at the beginning of the runs and slightly increased during irradiation, as a consequence of the accumulation of products in the gas phase.

Three consecutive irradiation cycles were always performed for each photocatalyst bed, in order to check the reproducibility of the photoactivity tests, with 30-min N₂ purging in the dark between each irradiation cycle. No remarkable variation in the rate of products formation in the gas phase was ever observed, which was thus evaluated as the average value in the three runs. In some cases, the same photocatalyst bed was tested also on the next day in three more subsequent irradiation cycles, with no significant variation in photoactivity.

3. Results and discussion

3.1. Photocatalysts characterisation

Both FP-made materials, with or without Pt, consisted of micro-aggregates of single crystal nanospheres, 10–25 nm in diameter, as revealed by HRTEM analysis (Fig. 1A), and displayed almost identical surface areas ($70 \text{ m}^2 \text{ g}^{-1}$ from BET analysis) and crystal phase

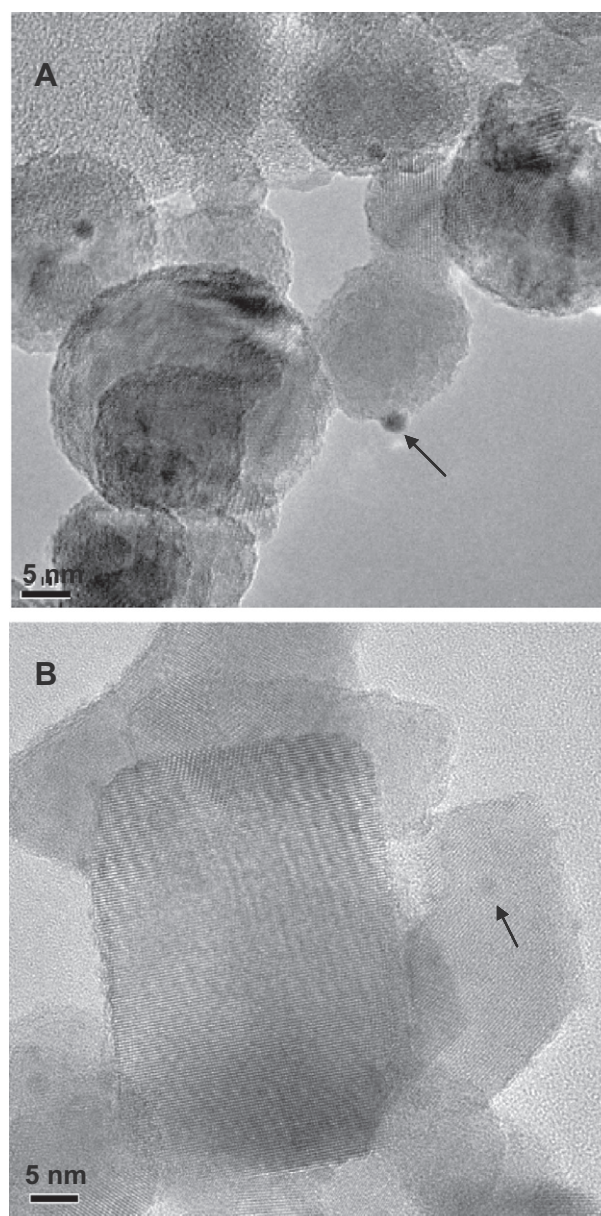


Fig. 1. HRTEM images of: (A) FP-0.5%Pt/TiO₂ and (B) 1%Ag/TiO₂. The arrows point to the noble metal nanoparticles.

composition (ca. 53% anatase and 47% rutile, from XRD analysis). The high rutile content is mainly due to the high temperature of the flame (ca. 2000 °C) [24], when xylene is used as solvent. The typical structure features of commercial P25 TiO₂, consisting of widely condensed, irregularly shaped, ca. 20 nm in size crystalline aggregates, was maintained after NM nanoparticles' deposition (see for example Fig. 1B). Also, the specific surface area, 48 m² g⁻¹ according to our BET analysis, and mixed crystal phase composition of ca. 80% anatase and 20% rutile, according to XRD measurements, were not altered by the here adopted low temperature noble metals' deposition procedure.

The STEM–HAAD images of the FP-made Pt/TiO₂ sample displayed in Fig. 2A evidence the presence of well-dispersed, ca. 1.5–3-nm-sized Pt nanoparticles, appearing as bright dots deposited on TiO₂, due to the different Z-contrast of the noble metal with respect to the titania support. By contrast, the 0.5%Pt/FP-TiO₂ (not shown), 0.5%Pt/TiO₂ (Fig. 2B) and 1%Pt/TiO₂ (Fig. 2C) samples prepared by the deposition of preformed Pt nanoparticles on FP-TiO₂ or P25 TiO₂ exhibit the same Pt particles size distribution (5–6 nm), with some extent of aggregation. Thus, the FP method allows the direct synthesis of noble metal-deposited materials, with

smaller and better dispersed NM nanoparticles, on a relatively higher surface area. No NM particle aggregation was observed in the case of 1%Au/TiO₂ (Fig. 2D), 1%Ag/TiO₂ (Fig. 2E) and 1%Au–1%Ag/TiO₂ (Fig. 2F). However, the gold-containing sample exhibits bigger NM nanoparticles (3–8 nm on average, together with some rare bigger particles up to 20 nm) than the silver-containing one (1.5–3 nm). The Z-contrast of silver is poorer than those of gold and platinum, silver being a lighter element. Finally, much bigger NM particles, ranging from 5 to 20 nm, were detected in 1%Au–1%Ag/TiO₂, and two types of surface nanoparticles could be distinguished in this case, *i.e.* bigger and brighter ones made of Au–Ag alloy, together with some smaller and less bright ones consisting of pure silver, as confirmed by the EDX analysis reported in Fig. 3.

The UV–vis absorption spectra of the Au, Ag and Au–Ag alloy colloidal suspensions before deposition on P25 are reported in Fig. 4A. They exhibit the plasmonic bands centred at 400 and at 530 nm, typical of colloidal silver and gold nanoparticles, respec-

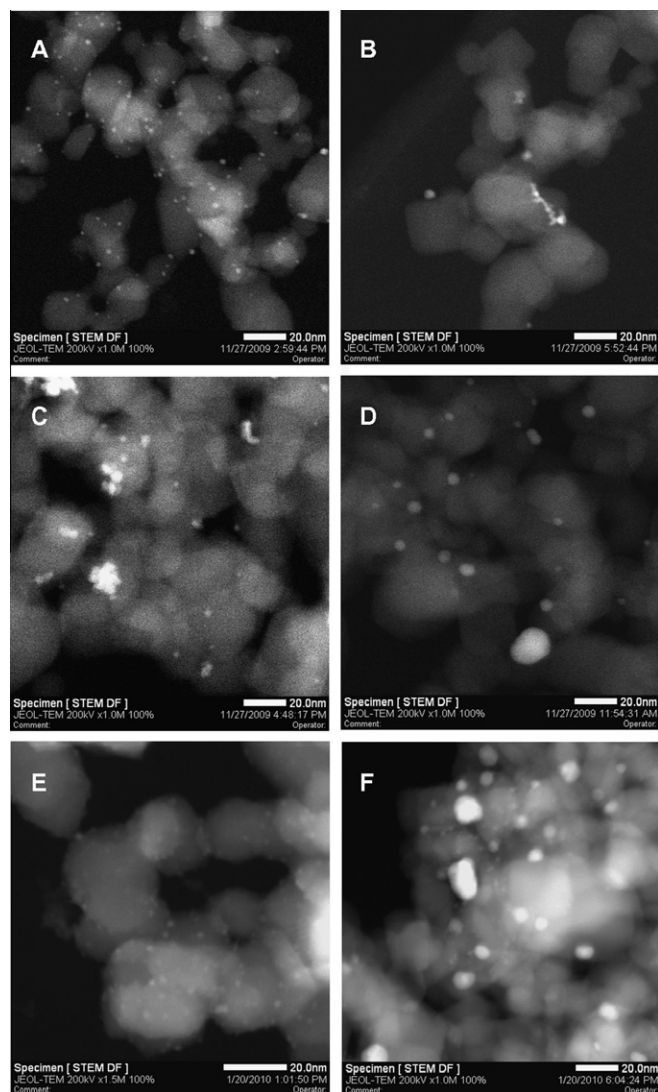


Fig. 2. STEM–HAADF images of: (A) FP-0.5%Pt/TiO₂, (B) 0.5%Pt/TiO₂, (C) 1%Pt/TiO₂, (D) 1%Au/TiO₂, (E) 1%Ag/TiO₂ and (F) 1%Au–1%Ag/TiO₂. Noble metal nanoparticles appear as bright dots on the titania support because of their higher Z-contrast.

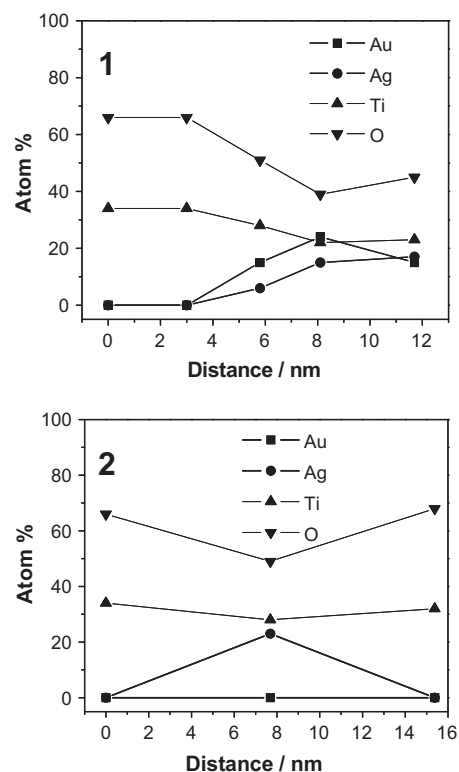
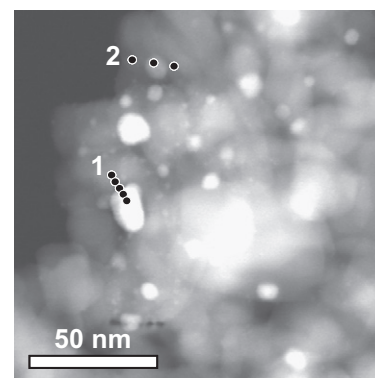


Fig. 3. STEM image of 1%Au–1%Ag/TiO₂ and EDX analysis (lower panels) of areas 1 and 2 outlined in the STEM image, showing the per cent atom composition moving along the marked points on: (1) an Au–Ag alloy nanoparticle and (2) a pure silver nanoparticle.

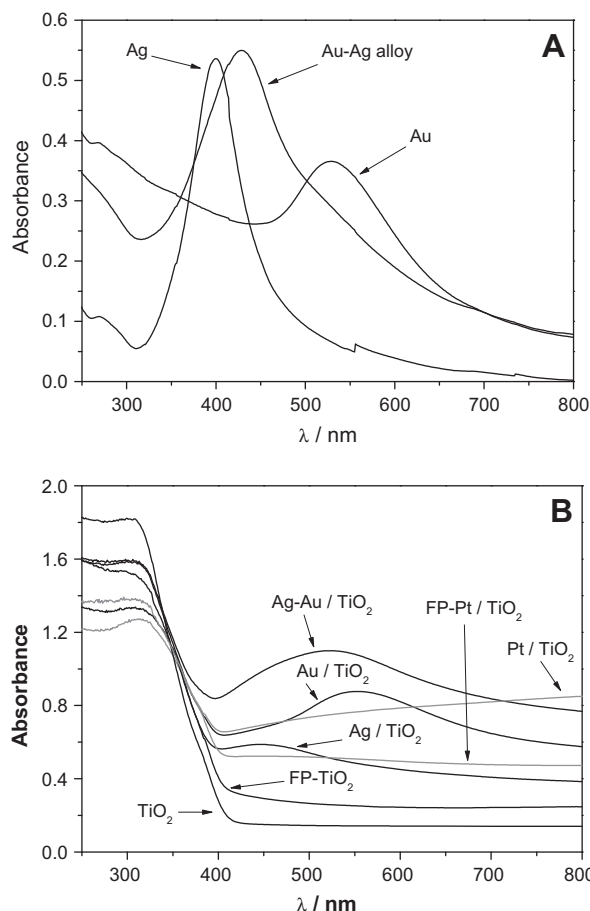


Fig. 4. UV-vis absorption spectra of: (A) Au, Ag and Au–Ag alloy colloidal aqueous suspensions; (B) TiO₂, FP-TiO₂, FP-0.5%Pt/TiO₂, (labelled as FP-Pt/TiO₂) and 1%M/TiO₂ (M = Au, Ag, Au–Ag and Pt) powders, recorded in reflectance mode.

tively [25], arising from the collective oscillation of free conduction band electrons, induced by interaction with an incident electromagnetic radiation, whose wavelength far exceeds the particles size. The Ag–Au alloy colloidal suspension shows a single plasmonic band centred at 430 nm, *i.e.* intermediate between those of pure Au and Ag colloids, confirming the formation of an alloy.

All of the investigated TiO₂-based photocatalysts exhibit a band gap adsorption threshold below 400 nm (Fig. 4B); metal-containing samples also exhibit plasmonic bands in the visible region, centred at 555 nm for Au, 445 nm for Ag and 525 nm for the Au–Ag alloy, *i.e.* all of them red-shifted compared to that of the corresponding colloidal suspension, indicating electronic interaction between NM nanoparticles and TiO₂ support. Pt/TiO₂ samples, appearing as a grey powders, exhibit a broad absorption in the visible region, without any specific plasmonic band.

3.2. Photocatalytic tests

3.2.1. Identification of products and intermediate species

Besides the two main photoreaction products, *i.e.* hydrogen and carbon dioxide, the presence of formaldehyde, carbon monoxide, dimethyl ether, methyl formate, acetaldehyde and traces of methane and ethane as by-products, was detected during all photocatalytic tests. Fig. 5 displays the typical composition vs. time profiles of the recirculating gas during irradiation, obtained when testing FP-made 0.5%Pt/TiO₂. The concentration of water and methanol (Fig. 5A) did not significantly vary under steady-state conditions, due to their low per cent conversion. The concentration

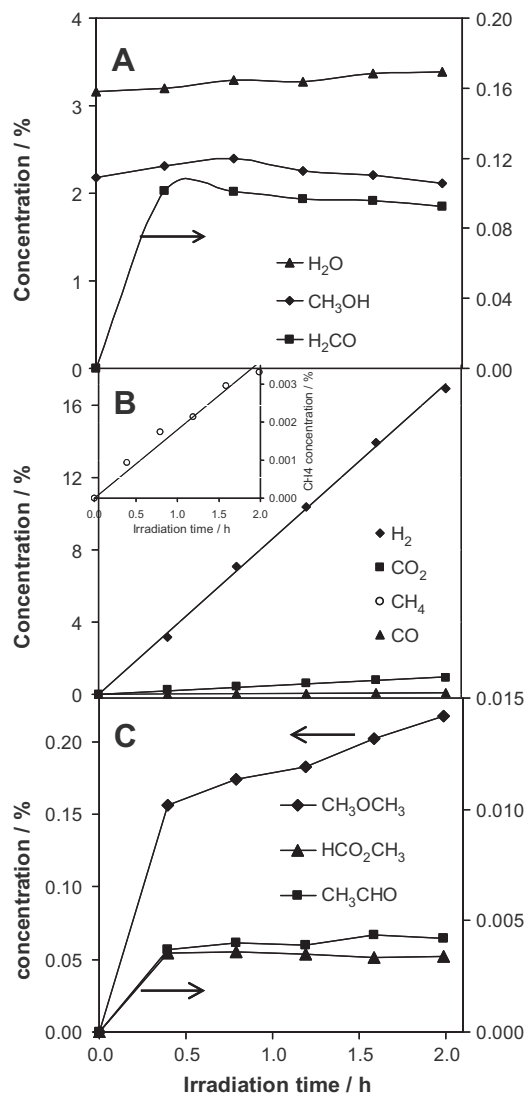
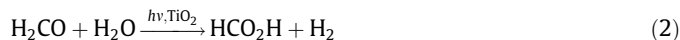
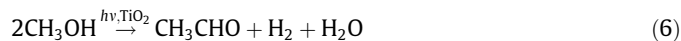
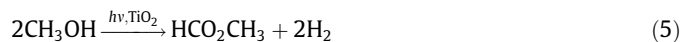


Fig. 5. Typical gas-phase composition profiles (concentration expressed in mole per cent) during irradiation, in the methanol photo-steam reforming reaction. Inset: magnification of the methane concentration profile. Specific reaction conditions: 0.014 g of FP-0.5%Pt/TiO₂ photocatalyst fed in recirculation mode with 40 mL min⁻¹ of 2% CH₃OH/3% H₂O/N₂ (balance) gas mixture.

of H₂, CO₂, CO and CH₄ (Fig. 5B) increased linearly with time because they accumulated in the recirculating gas phase, according to a pseudo-zero order rate law, due to the high excess of reactants. By contrast, the concentration of formaldehyde, methyl formate, acetaldehyde and dimethyl ether (Fig. 5A and C) rapidly increased at the beginning of irradiation and then remained almost constant in the gas phase, because such species accumulated in the methanol–water liquid solution when the gas phase bubbled into it, as confirmed by GC analysis of the liquid at the end of photocatalytic tests. Formic acid, another possible intermediate species, was never detected by GC analysis of the gas phase, very likely because its amount always remained below the detection limit. However, its formation and accumulation in the liquid solution was confirmed by IC analysis at the end of the runs.

On the basis of the main final oxidation products, by-products and intermediate species detected in both gas and liquid phase, the following reaction scheme should be considered:





According to reaction (7), the formation of dimethyl ether does not contribute to hydrogen production.

The results of photocatalytic tests performed with the investigated photocatalysts series are reported in Table 1. The rates of H_2 , CO_2 , CO and CH_4 production were taken as the slope of the straight lines of the produced amount (normalised per unit catalyst weight) vs. irradiation time plots (see for example Fig. 5B). The rate of formaldehyde production ($r_{\text{H}_2\text{CO}}$) was estimated by the average GC peak area recorded in gas samples collected during irradiation at the exit of the photoreactor, taking into account the flow rate of the recirculating gas, under the very reasonable assumption that almost all formaldehyde present in the gas phase at the exit of the photoreactor was trapped by the methanol/water solution and not fed back into the photoreactor. The average rate of formic acid production was estimated as the overall amount accumulated into the liquid solution, determined by IC at the end of the runs, divided by the overall irradiation time and the weight of catalyst, thus assuming a constant production rate during irradiation also for this intermediate species.

The selectivity in hydrogen production was also calculated from the rates of H_2CO , HCO_2H , CO or CO_2 formation, as the ratio between the rate of H_2 production from methanol to give one of the four products, by taking into account the stoichiometric coefficients of reactions (1)–(4), and the overall rate of H_2 photoproduction. For example, the selectivity of CO_2 in H_2 production (S_{CO_2}) was calculated as follows:

$$S_{\text{CO}_2} = \frac{3 \cdot r_{\text{CO}_2}}{r_{\text{H}_2}} \cdot 100$$

The sum of the so obtained selectivity values, also reported in Table 1, is always close to 100%, indicating a very good mass balance agreement. Thus, under standard experimental conditions, the contribution to H_2 production of reactions (5) and (6) is negligible. However, this does not apply for higher methanol to water molar ratios, as will be discussed in Section 3.2.3.

3.2.2. Effects of noble metals deposition on TiO_2

The rate of hydrogen production r_{H_2} on flame-made TiO_2 was higher than on unmodified TiO_2 P25, as already observed in our previous studies [18], and it dramatically increased upon noble metals' deposition on the semiconductor oxide, as clearly evidenced by the overview, reported in Fig. 6, of the hydrogen production rate and selectivity values obtained with the investigated photocatalysts. Silver resulted the less effective co-catalyst, with only a fourfold r_{H_2} increase with respect to r_{H_2} on bare P25 TiO_2 , whereas r_{H_2} increased by 37 and 52 times when the same amount of gold or platinum, respectively, was deposited on TiO_2 . The difference in the photocatalytic performance of the three metal co-catalysts can be related to their work function values (Φ), i.e. the energy required to promote an electron from the Fermi energy level into vacuum (the higher is Φ , the lower in energy is the Fermi level). In fact, the greater is the difference between the metal work function and that of the TiO_2 support, the higher is the Schottky barrier [8,9], the electronic potential barrier generated by the band alignment at the metal–semiconductor heterojunction, with consequent increased efficiency of photogenerated electron transfer and trapping by the metal, leading to higher r_{H_2} . For the 111 crystal

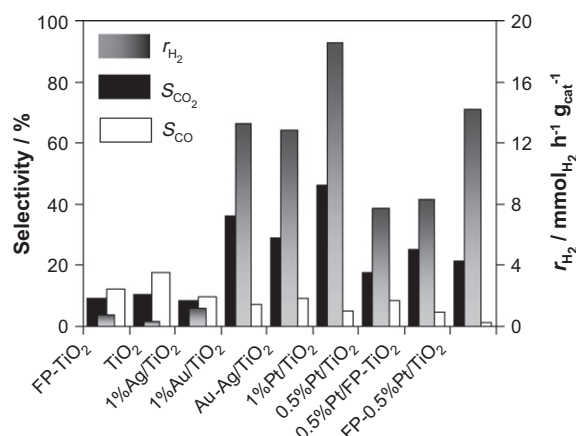


Fig. 6. Overview of the rate of hydrogen production, r_{H_2} , and per cent selectivity to CO_2 and to CO obtained with the investigated photocatalysts. Reaction conditions are reported in Table 1.

plane, $\Phi = 4.74$ eV for Ag, $\Phi = 5.31$ eV for Au and $\Phi = 5.93$ eV for Pt [26], whereas Φ values of 4.6–4.7 eV are reported in literature for TiO_2 [27]. Consequently, Pt is a more efficient electron trapper than gold, in line with the higher photoactivity of Pt-modified TiO_2 . By contrast, the Φ value of Ag, very close to that of TiO_2 , suggests scarce electron transfer, resulting in less efficient charge separation and consequent little improvement in the photocatalytic performance upon Ag addition to TiO_2 .

The same trend is reflected by r_{CO_2} and S_{CO_2} in the series of photocatalysts containing 1% metal on P25 TiO_2 (see Fig. 6), 1%Pt/ TiO_2 being the most selective photocatalyst (46%), followed by 1%Au/ TiO_2 (36%) and 1%Ag/ TiO_2 (8%). Moreover, when considering the use of hydrogen as a feedstock for fuel cells, CO certainly is the most undesired by-product, being a well-known poison for the Pt-based catalysts in fuel cells. From the point of view of CO production, bare TiO_2 is the less performing photocatalyst, not only because of the low r_{H_2} value, but also for its high S_{CO} value, even higher than S_{CO_2} (e.g. 18% vs. 11% for TiO_2 P25, see Table 1). Noble metal deposition on TiO_2 significantly increases S_{CO_2} and decreases S_{CO} . In particular, 1%Pt/ TiO_2 showed the lowest S_{CO} , followed by Au/ TiO_2 and Ag/ TiO_2 . This clearly indicates that the more efficient is the separation between photoproduced charge carriers in the photocatalyst, the more efficient are not only the e_{CB}^- -involving reduction paths, mainly leading to H_2 production, but also the h_{VB}^+ -initiated complete CH_3OH oxidation to CO_2 .

Although a systematic investigation into the effects of metal loading on titania is beyond the scope of the present work, we notice that a more than doubled r_{H_2} value was attained, when the amount of Pt deposited on TiO_2 P25 was doubled from 0.5% and 1% (Fig. 6), and even more remarkable was the effect observed in r_{CO_2} and S_{CO_2} values (Table 1), increasing from 0.45 ($S_{\text{CO}_2} = 17.5\%$) to 2.88 $\text{mmol}_{\text{CO}_2} \text{h}^{-1} \text{g}_{\text{cat}}^{-1}$ ($S_{\text{CO}_2} = 46.4\%$).

A comparison between the performance of the three 0.5 wt.%Pt-containing photocatalysts, prepared either by deposition of preformed metal nanoparticles on P25 TiO_2 and on FP- TiO_2 , or by one-step FP (FP-0.5%Pt/ TiO_2 , see Fig. 6), evidences that, although bare FP- TiO_2 was more active than P25, much more closer r_{H_2} values were attained when the same amount of Pt was deposited on the two TiO_2 supports, with a similar metal nanoparticles size distribution, whereas r_{CO_2} and r_{CO} varied more significantly (Table 1). Indeed, as in the case of the bare photocatalysts, 0.5%Pt/FP- TiO_2 ensured higher r_{CO_2} and S_{CO_2} values and lower r_{CO} and S_{CO} values than 0.5%Pt/ TiO_2 . These observations could be explained by considering that H_2 is expected to be mainly produced through the involvement of photopromoted electrons on the NM nanoparticles surface,

which are preformed before deposition on TiO₂. Therefore, they are similar for the two 0.5%Pt/TiO₂ and 0.5%Pt/FP-TiO₂ photocatalysts, and this leads to similar r_{H_2} values. On the other hand, methanol photo-oxidation, involving valence band holes, occurs on the titania surface, and this explains why the noble metal-modified photocatalysts retain memory of the higher photoactivity of bare TiO₂. Finally, the one-step prepared FP-0.5%Pt/TiO₂ exhibited an exceptionally higher performance with respect to those of the two materials prepared by deposition of preformed Pt nanoparticles, despite of the same noble metal content, with doubled r_{H_2} and r_{CO_2} values, together with an exceptionally low r_{CO} value and only 1% selectivity to CO. The higher photoactivity of FP-0.5%Pt/TiO₂ is most probably a consequence of the lower Pt particle size and higher Pt dispersion on the TiO₂ surface (see Fig. 2A), typical of flame-made catalysts, ensuring a more extended Pt surface area, in line with the r_{H_2} increase and r_{CO} decrease with decreasing the Au particles' size on TiO₂ in the liquid-phase methanol photo-reforming over Au/TiO₂ photocatalysts [10].

Silver was the least performing co-catalyst on TiO₂ (Fig. 6), and its addition to gold to form Au–Ag alloy nanoparticles induced a decrease in photoactivity with respect to that of pure gold nanoparticles on TiO₂. Indeed, the r_{H_2} and selectivity to CO₂ values attained with the 1%Au–1%Ag/TiO₂ photocatalyst were lower than the corresponding values attained with 1%Au/TiO₂, with a slightly higher selectivity to CO. It is reasonable to assume that silver addition induced a work function decrease with respect to that of pure gold, leading to less efficient separation of the photoproduced charge pairs.

Finally, the rate of formation of the other reduction product, i.e. methane, was always very low with respect to that of hydrogen production r_{H_2} , and it only slightly increased upon noble metal deposition (Table 1). This might be an indication that photopromoted electrons are not directly involved in methane formation. On the other hand, formaldehyde was always the main by-product formed on NM containing photocatalysts, with a selectivity always exceeding 40%, except in the case of 1%Pt/TiO₂, mainly yielding CO₂.

3.2.3. Effect of methanol and water partial pressures

In order to ascertain how the rates of product formation are influenced by the methanol/water molar ratio in the recirculating gas phase under irradiation, and in particular to discern the role of water in hydrogen production and methanol oxidation, a systematic investigation was performed by varying the methanol and water partial pressures. The rate of formation of the main reaction products was thus measured by feeding the FP-0.5%Pt/TiO₂ photocatalyst with vapours in equilibrium with water/methanol liquid solutions, kept at 30 °C, containing different methanol molar

fractions x ($0.0045 \leq x \leq 1$). At this temperature, the vapour pressure of methanol and water are 163.97 and 31.82 mm Hg, respectively; their partial pressure ratios in the gas phase, $p_{\text{H}_2\text{O}}/p_{\text{CH}_3\text{OH}}$, were calculated by assuming an ideal behaviour, according to Raoult's law. The complete series of results concerning H₂, CO₂, CO, H₂CO, HCO₂H and CH₄ formation rates and selectivities in H₂ production is reported in Table 2. The effects of the fed mixture composition on the rate of formation of each product can better be appreciated in Fig. 7, where rate values are plotted as a function of x , the molar fraction of methanol in the liquid phase.

Fig. 7 clearly shows that the rates of hydrogen, formaldehyde and formic acid production display bell-shaped curves as a function of x , whereas carbon dioxide exhibits a hyperbolic decay curve with increasing x . Thus, the rate of CO₂ production and the selectivity to CO₂ were high at relatively high water partial pressure and rapidly decreased as the partial pressure of water decreased and that of methanol increased, clearly showing that water is needed to achieve complete CH₃OH oxidation. On the other hand, the rate of H₂ production increased with increasing x , reaching a sort of plateau (ca. 17 mmol_{H₂} h⁻¹ g_{cat}⁻¹) for $0.2 < x < 0.6$, and decreased down to 2.8 mmol_{H₂} h⁻¹ g_{cat}⁻¹, when the photocatalyst bed was fed with pure methanol. It is worth underlining, however, that whereas hydrogen and formaldehyde production did not drop to zero under such conditions, no HCO₂H and CO₂ were produced in the absence of water, in agreement with reaction (2), followed by reaction (3). By contrast, the rate of CO production was almost constant up to $x = 0.8$, and it dropped to ca. zero when pure methanol was fed to the photocatalyst, with the selectivity to CO never exceeding 1.5%. Furthermore, CO production rate as a function of x has a trend more similar to that of formic acid production, than to that of formaldehyde production, which did not drop to zero in the absence of water. This indicates that CO does not form directly from methanol, but it only forms from methanol oxidation intermediates, and in particular mainly through formic acid dehydration, reaction (8), rather than through formaldehyde oxidation, reaction (4).



The two CH₃CHO and HCO₂CH₃ by-products exhibit a null production rate at low x and a production rate increase for $x > 0.1$, with a maximum rate shifted towards very high x values (ca. 0.9). This trend is consistent with reactions (5) and (6), involving two adjacent surface-adsorbed methanol molecules, because with increasing x and methanol partial pressure, the surface coverage by methanol increased, together with the probability that two vicinal adsorbed methanol molecules interact with each other, rather than with water. However, CH₃CHO and HCO₂CH₃ production from pure methanol occurred at lower rate, suggesting that water plays a role also in their formation.

Table 2
Effect of methanol molar fraction in the aqueous solution, $x_{\text{CH}_3\text{OH}}$, and of water-to-methanol partial pressure ratio in the recirculating gas phase in the photocatalytic performance of FP-0.5%Pt/TiO₂ in terms of rates of products formation, r , and per cent selectivity in relation to hydrogen production, S .

$x_{\text{CH}_3\text{OH}}$	$\frac{p_{\text{H}_2\text{O}}}{p_{\text{CH}_3\text{OH}}}$	Production rate (mmol h ⁻¹ g _{cat} ⁻¹)						Selectivity in H ₂ production (%)				
		H ₂	CO ₂	CO	H ₂ CO	HCO ₂ H	CH ₄	CO ₂	CO	H ₂ CO	HCO ₂ H	Sum
1.000	0	2.81	0	0.003	1.75	0	0	0	0.22	62.3	0	63
0.956	0.009	6.18	0.03	0.026	3.42	0.18	0	1.7	0.83	55.4	5.8	64
0.894	0.023	8.71	0.10	0.061	4.66	0.35	0	3.0	1.40	53.5	8.1	66
0.800	0.05	12.74	0.16	0.078	5.49	0.40	9.6×10^{-4}	3.7	1.23	43.1	6.3	54
0.640	0.11	16.76	0.32	0.071	8.03	1.14	1.6×10^{-3}	5.8	0.85	47.9	13.6	68
0.400	0.29	17.38	0.54	0.076	9.10	1.62	1.8×10^{-3}	9.3	0.88	52.3	18.6	81
0.229	0.66	16.63	0.80	0.064	9.49	1.98	2.0×10^{-3}	14.4	0.77	57.1	23.8	96
0.100	1.75	14.23	1.02	0.078	7.85	1.18	2.3×10^{-3}	21.6	1.10	55.1	16.6	94
0.047	3.93	12.77	1.45	0.086	5.40	1.05	2.2×10^{-3}	34.1	1.35	42.3	16.4	94
0.023	8.30	11.43	1.82	0.065	4.25	0.79	2.4×10^{-3}	47.8	1.14	37.2	13.8	100
0.0090	21.4	9.98	1.99	0.067	2.96	0.34	3.2×10^{-3}	59.9	1.34	29.7	6.8	98
0.0045	43.2	9.17	2.35	0.067	1.41	0.26	4.5×10^{-3}	76.7	1.45	15.3	5.7	99

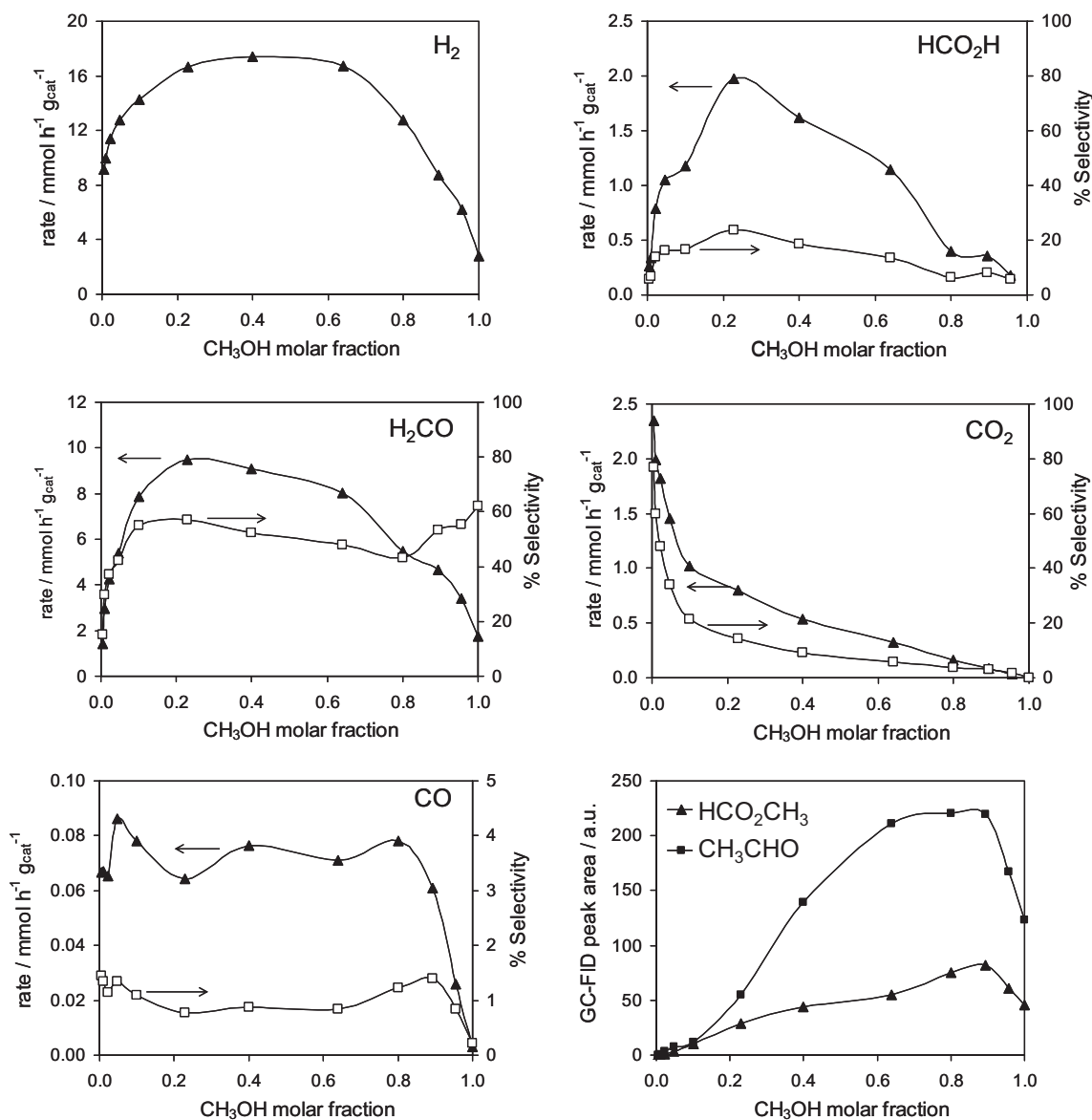


Fig. 7. H₂, H₂CO, HCO₂H, CO₂, CO, HCO₂CH₃ and CH₃CO production rates (▲) and per cent selectivity in relation to hydrogen production (□) obtained with the FP-0.5%Pt/TiO₂ photocatalyst, as a function of the methanol molar fraction in the aqueous solution.

Finally, the sum of the selectivity S_{CO_2} , S_{CO} , $S_{\text{H}_2\text{CO}}$ and $S_{\text{HCO}_2\text{H}}$ values (Table 2, last column on the right) gives a good mass balance for the overall reactions, *i.e.* this sum approaches 100%, only for low x values, indicating that reactions (1)–(4) relative to overall photocatalytic steam reforming, satisfactorily accounts for hydrogen production and simultaneous oxidation products, whereas this sum decreases for $x > 0.4$, *i.e.* when the contribution of bimolecular side-reactions (5) and (6) to hydrogen production becomes significant.

3.2.4. Effect of water on the gas-phase anaerobic oxidation of formic acid

In order to have a better insight into the role played by water in the final steps of the investigated reaction, and in particular on the origin of CO production, we performed some tests on the effect of water in the anaerobic photo-oxidation of formic acid, one of the intermediate species of methanol oxidation. The rates of hydrogen, carbon dioxide and carbon monoxide production were thus measured with the FP-0.5%Pt/TiO₂ photocatalyst fed with vapours in equilibrium with liquid phases, kept at 30 °C: (i) pure formic acid

($x_{\text{HCO}_2\text{H}} = 1.0$); (ii) 80 vol.% HCO₂H/H₂O ($x_{\text{HCO}_2\text{H}} = 0.7$); and (iii) 20 vol.% HCO₂H/H₂O ($x_{\text{HCO}_2\text{H}} = 0.1$).

The results, shown in Fig. 8, first of all demonstrate that both H₂ and CO₂ production rates significantly increased with increasing the water partial pressure in the reaction mixture. Furthermore, the rate of hydrogen production was always higher than that of CO₂ production. Both facts clearly point to an involvement of water molecules in the photocatalytic oxidation of formic acid in the absence of dioxygen. In fact, if only formic acid was involved in a simultaneous oxidation and reduction process according to reaction (3), equal amounts of H₂ and CO₂ would have been produced under irradiation. So, a much more complex mechanism is at work, part of the photoproduced hydrogen deriving from water (protons) reduction by photopromoted electrons, most probably occurring on the NM nanoparticles, whereas formic acid may undergo oxidation either through a direct mechanism, by interaction with photo-produced valence band holes, or through the attack of ·OH radical produced from water oxidation on the irradiated photocatalyst surface [2]. The difference between the rates of H₂ and CO₂ production observed for $x_{\text{HCO}_2\text{H}} = 1$ might be accounted for by the pres-

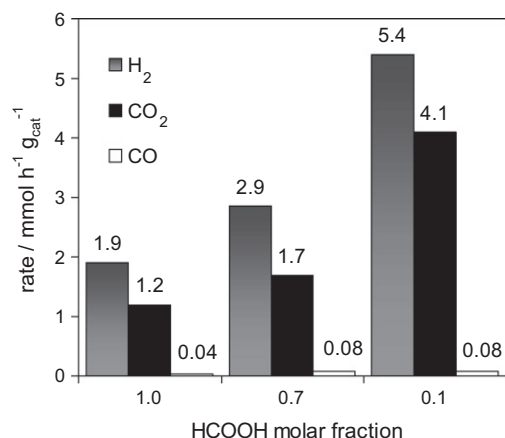


Fig. 8. H₂, CO₂ and CO production rates in the gas-phase anaerobic photo-oxidation of formic acid on the FP-0.5%Pt/TiO₂ photocatalyst, fed with vapours of pure formic acid or formic acid/water solutions.

ence of the small amount of water (*ca.* 2%) in the employed formic acid.

Finally, the rate of CO production from pure HCO₂H was much higher than that from pure CH₃OH (0.04 vs. 0.003 mmol_{CO} h⁻¹ g_{cat}⁻¹), and it also increased in the presence of water (Fig. 8), reaching a value of *ca.* 0.08 mmol_{H₂} h⁻¹ g_{cat}⁻¹. This is in agreement with the above proposed mechanism of CO production in the process under study, also in line with Wu's results [10], i.e. CO is formed preferentially from formic acid through reaction (8). Water has a beneficial effect also on this reaction, most probably by providing ·OH radical-mediated alternative paths.

4. Conclusions

FP-made photocatalysts containing NM nanoparticles are best performing in the photo-steam reforming of methanol, in terms of both hydrogen production efficiency and low CO production, because of their smaller NM particle size and higher dispersion on an oxide higher surface area. Pt confirmed to be the most effective co-catalyst also for this gas phase reaction, followed by gold and silver, in agreement with their work function values.

Although the presence of methanol, as an electron donor, is beneficial in the photocatalytic hydrogen production from water, its amount in the fed gas mixture should be kept low, the highest hydrogen production rate being attained for water-to-methanol molar ratios in the feeding gas phase comprised between 0.1 and

0.7. Complete methanol oxidation to CO₂ very rapidly declines with increasing methanol amount, starting from very low methanol content. Carbon monoxide is mainly produced from formic acid dehydration.

Acknowledgments

Financial support from the University of Milan PUR funds, within the Project *Photoinduced Redox Processes on Semiconductor Surfaces* and from the CARIPLO Foundation through the Project *Development of nanostructured photocatalytic films for energy conversion on microplatforms* is gratefully acknowledged.

References

- [1] K. Weissermel, H.J. Arpe, *Industrial Organic Chemistry*, fourth ed., Wiley-VCH, Weinheim, 2003.
- [2] A. Fujishima, X. Zhang, D.A. Tryk, *Surf. Sci. Rep.* 63 (2008) 515.
- [3] Z. Zou, J. Ye, K. Sayama, H. Arakawa, *Nature* 414 (2001) 625.
- [4] Z. Zou, H. Arakawa, *J. Photochem. Photobiol. A* 158 (2003) 145.
- [5] R. Abe, M. Higashi, K. Sayama, Y. Abe, H. Sugihara, *J. Phys. Chem. B* 109 (2005) 16052.
- [6] W. Yao, J. Ye, *Chem. Phys. Lett.* 435 (2007) 96.
- [7] H. Kato, A. Kudo, *Catal. Today* 78 (2003) 561.
- [8] P. Kamat, *J. Phys. Chem. B* 106 (2002) 7729.
- [9] A.L. Linsebigler, G. Lu, J.T. Yates, *Chem. Rev.* 95 (1995) 735.
- [10] G. Wu, T. Chen, W. Su, G. Zhou, X. Zong, Z. Lei, C. Li, *Int. J. Hydrogen Energy* 33 (2008) 1243.
- [11] O. Rosseler, M.V. Shankar, M. Karkmaz-Le Du, L. Schmidlin, N. Keller, V. Keller, *J. Catal.* 269 (2010) 179.
- [12] N. Strataki, V. Bekiari, D.I. Kondarides, P. Lianos, *Appl. Catal. B: Environ.* 77 (2007) 184.
- [13] J. Greaves, L. Al-Mazroai, A. Nuhu, P. Davies, M. Bowker, *Gold Bull.* 39 (2006) 216.
- [14] M. Kang, *J. Mol. Catal. A: Chem.* 197 (2003) 173.
- [15] H. Yoshida, K. Hirao, J. Nishimoto, K. Shimura, S. Kato, H. Itoh, T. Hattori, *J. Phys. Chem. C* 112 (2008) 5542.
- [16] G.L. Chiarello, I. Rossetti, L. Forni, *J. Catal.* 236 (2005) 251.
- [17] G.L. Chiarello, E. Selli, L. Forni, *Appl. Catal. B: Environ.* 84 (2008) 332.
- [18] G.L. Chiarello, L. Forni, E. Selli, *Catal. Today* 144 (2009) 69.
- [19] J.H. Liu, A.Q. Wang, Y.S. Chi, H.P. Lin, C.Y. Mou, *J. Phys. Chem. B* 109 (2005) 40.
- [20] M.D. Advanced Selected Powder Diffraction Data, J.C.P.D.S., Swarthmore, PA, 1974.
- [21] H.M. Rietveld, *J. Appl. Cryst.* 2 (1969) 65.
- [22] A. Altomare, M.C. Burla, C. Giacovazzo, A. Guagliardi, A.G.G. Moliterni, G. Polidori, R. Rizzi, *J. Appl. Cryst.* 34 (2001) 392.
- [23] C.G. Hatchard, C.A. Parker, *Proc. Roy. Soc. (London)* A235 (1956) 518.
- [24] G.L. Chiarello, I. Rossetti, P. Lopinto, G. Migliavacca, F. Forni, *Catal. Today* 117 (2006) 549.
- [25] M.M. Alvarez, J.T. Khoury, T.G. Schaaff, M.N. Shafiqullin, I. Vezmar, R.L. Whetten, *J. Phys. Chem. B* 101 (1997) 3706.
- [26] CRC Handbook of Chemistry and Physics, 87th ed., Taylor & Francis, 2006, pp. 12–114.
- [27] C. Young, T.M. Lim, K. Chiang, J. Scott, R. Amal, *Appl. Catal. B: Environ.* 78 (2008) 1.